Arch. Min. Sci. **63** (2018), 2, 251-268

Electronic version (in color) of this paper is available: http://mining.archives.pl

DOI 10.24425/122446

PAWEŁ WRONA*#, ALEKASANDER KRÓL*, MAŁGORZATA KRÓL*

GAS OUTFLOW FROM AN UNDERGROUND SITE – NUMERICAL SIMULATIONS INTO BARIC TENDENCY AND AIRFLOW RATE RELATIONSHIP

EMISJA GAZÓW Z GÓROTWORU – SYMULACJE NUMERYCZNE WPŁYWU TENDENCJI BARYCZNEJ NA INTENSYWNOŚĆ PRZEPŁYWU GAZÓW

Gas emissions from underground sites to the atmosphere depend on many factors. Pressure drops are considered to be the most important. However, emissions can also be observed during the initial phase of the pressure rise, following a previous drop in pressure. On the other hand, gas emissions may not be detected when the pressure drops, especially when a previous pressure rise has taken place.

The aim of the research was to determine the role of variations in baric tendency on airflow rate and its direction.

To solve this problem a numerical model was built utilizing the Ansys Fluent software package. Subsequently, three scenarios of baric tendency variations were tested: a) rise – drop, b) drop – drop, c) drop – rise.

The results showed inert behavior of gases. Under scenario (c), 1 hour after the change in tendency gases still were flowing out to the atmosphere.

Considering scenario (a), it was proved that even during a pressure drop gas emissions do not take place, which can be crucial for further determination of the gas hazard at the surface or for assessment of the rate of gas emissions from a particular gas emitter.

Scenario (b) merely gave an overview of the process and was mainly used for validation purposes. It gave a maximal CO_2 concentration of 2.18%vol (comparable to measurements) and a CO_2 mass flow rate 0.15kg/s. Taking into account greenhouse gas emissions this amounted to 514 kg CO_2/h.

Keywords: CFD simulation, CO_2 leak, Ansys Fluent, environmental impact, gas hazard

Emisja gazów z górotworu do atmosfery zależy od wielu czynników, z których jako najważniejszy uznawane są spadki ciśnienia atmosferycznego. Jednakże podczas prowadzonych badań wypływ gazów został także odnotowany podczas początkowego okresu zwyżki barycznej, poprzedzonego zniżką. Wystąpiło także zjawisko braku wypływu gazów mimo występującej zniżki barycznej, w szczególności po okresie wzrostu ciśnienia.

Dlatego celem przeprowadzonych badań było określenie wpływu zmian ciśnienia atmosferycznego (rodzaju tendencji barycznej) na natężenie przepływu gazów pomiędzy górotworem a atmosferą oraz

* SILESIAN UNIVERSITY OF TECHNOLOGY, POLITECHNIKA ŚLĄSKA, AKADEMICKA 2 ST. 44-100 GLIWICE, POLAND

Corresponding author: pawel.wrona@polsl.pl

wyznaczenie jego kierunku. Do badań stworzono model numeryczny zjawiska w programie Ansys Fluent. Założono trzy warianty zmian ciśnienia: a) zwyżka – zniżka, b) zniżka – zniżka, c) zniżka – zwyżka.

Otrzymane wyniki potwierdziły występującą bezwładność badanego procesu.

W przypadku scenariusza (c), 1 gazy wypływały do atmosfery przez okres godziny po zmianie tendencji barycznej ze zniżki na zwyżkę.

Rozpatrując scenariusz (a), dowiedziono, że emisja gazów może nie wystąpić mimo zachodzącej zniżki ciśnienia atmosferycznego. Może to mieć kluczowe znaczenie przy określaniu zagrożenia gazowego na powierzchni terenu lub wyznaczaniu intensywności emisji gazów z górotworu.

Scenariusz (b) był scenariuszem porównawczym i służył do walidacji modelu. Dla tego scenariusza otrzymano maksymalne stężenie CO_2 wynoszące 2.18%vol (wartość porównywalna ze stwierdzoną podczas pomiarów) oraz natężenie emisji CO_2 równe 0.15kg/s. W przeliczeniu na emisję godzinną jest to 514kg CO_2/h. Wartość ta ma znaczenie pod kątem emisji gazów cieplarnianych do atmosfery.

Słowa kluczowe: symulacja CFD, emisja CO_2, Ansys Fluent, oddziaływanie na środowisko, zagrożenie gazowe

1. Introduction

Gas emissions from underground sites to the atmosphere depend on many factors (Wrona et al., 2016). Nowadays, this issue is becoming more important due to mine closure and other environmentally friendly activities which are already planned or initiated in underground sites, e.g. Carbon Capture and Storage (CCS) (Lewicki et al., 2007; Annunziatellis et al., 2008). According to (Pawar et al., 2009; Schroder et al., 2016), leakage of CO_2 through plugged and abandoned wellbores is one of the major concerns for long-term safety and effectiveness of geologic CO_2 sequestration.

The process of gas outflow from underground sites is also observed after mine closure and it can be anticipated as a breakdown of an underground coal gasification installation (UCG) (Wrona et al. 2016). Uncontrolled gas emissions are also potential emergency situations during methane drainage.

In terms of environmental protection and gas hazards at the surface, two gases are the most important: carbon dioxide (CO_2) and methane (CH_4) (Bateson et al., 2008; Cheng et al., 2011; Beaubien et al., 2013; Lagny et al., 2013; Feitz et al., 2014; Jones et al., 2014). They are both considered to be greenhouse gases.

Modeling of the process is complicated due to having only partial knowledge of an underground site, especially when it was abandoned long time ago. The structure of underground excavations and the volume of voids can only be estimated on the basis of mining maps (if they are available). In addition, the process can only be monitored at the surface, mainly above closed shafts or in the area of faults (Wrona et al., 2016).

Taking into consideration the issues mentioned above, there are currently the following groups of gas flow models:

- models of CO_2 leakage (e.g. Paulley et al., 2013; Pawar et al., 2009).
- models of gas flow through a rock mass (e.g. Perera et al., 2011; Koyama et al., 2008, Oldenburg et al., 2010).
- models of gas flow in a mine ventilation network (e.g. Herran-Gonzales et al., 2009; Dziurzyński et al., 2008),
- models of gas flow or migration to the surface after mine closure (e.g. Lunarzewski, 2010).

The process strongly depends on pressure variations. These variations can be described by baric tendency, which is positive when pressure rises and negative when it falls. Baric tendency (later in the text: BT is given in Pa/3h or Pa/1h (Wrona et al., 2016).

Eicker (Eicker, 1987) stated that the relationship between airflow rate and pressure is linear, which was subsequently found to be incorrect.

The aim of the research was to estimate the variability of air velocity and its direction at the outlet of an underground reservoir under three different meteorological scenarios. The first was when pressure began to drop after a period of having risen, the second was when pressure continued to drop but with a different BT, and the third was when pressure started to rise after a drop period.

The time required for direction change was checked and the emissions rate was estimated.

Presently, there are many significant PC programs allowing simulations to be performed in the field of computational fluid dynamics (CFD). They can also be applied successfully to gas flow analysis. Ansys Fluent was selected for the research study due to its powerful capabilities for modeling fluid flow and heat exchange across a wide range of cases. This software is well recognized and widely used in many research and technical applications.

The model was validated by comparison with the measuring data.

2. Fluid movement – the physical principles of numerical analysis

Ansys Fluent solves fluid flow equations by the finite volume method (FVS). The first step is to divide a particular space (called as a domain) into a large number of small volumes (cells). "Finite volume" refers to a small volume surrounding each node point on a mesh. Balance equations are solved for each finite volume (for examined parameters) (1):

$$\frac{\partial}{\partial t}\int_V \rho\Phi dV + \int_A \rho\Phi\bar{u}d\bar{A} = \int_A \Gamma\nabla\Phi d\bar{A} + \int_V S_\Phi dV \tag{1}$$

An adequate balance equation depends on the value of Φ:

- balance of mass (continuity equation, $\Phi = 1$),
- balance of momentum (Φ represents velocity components u_x, u_y, u_z),
- balance of energy (Φ represents density of energy h).

The following parts of the balance equation describe changes in time, convectional transport, diffusive transport and the generation rate of Φ. The symbol ρ (in equation 1) represents the density, u denotes the local velocity of flow, Γ is the diffusion coefficient and S_Φ is the rate of creation of Φ. In the case of the balance of momentum equation, the second part consists of nonlinear elements (product of velocity components), which causes significant difficulties when solving the problem. This is because the solution may be unstable – a small change in input data can entirely change the nature of the solution.

Apart from balance equations, additional groups of equations are included in the solving process, e.g. boundary conditions, specification of applied materials, simplifications and approximations. Approximation equations refer to combustion models, evaporation and turbulence. The differential equations (adequate for each finite volume) are then replaced with difference ones and this creates the system of algebraic equations.

2.1. Modeling of turbulent flow in the shaft

Real flux in a shaft can be turbulent. For higher velocities, turbulence and the resulting eddies of varying size are expected. Considering time and space, the flow becomes chaotic.

Considering the engineering and practical applications, detailed knowledge about flux on a micro scale is not necessary. Average values of the velocity and energy of turbulence are sufficient as a result, and so some approximations are common: Large Eddy Simulation (LES) and Reynolds Averaged Navier-Stokes (RANS) models (Geurts, 2003).

The LES method is based on direct, numerical solution of the Navier-Stokes equations for the largest eddies, and the smallest eddies (with dimension smaller than one cell) are modelled (Vreman et al., 1997).

The RANS method averages Navier-Stokes equations in time and the results are in fact also averaged. It allows a decrease in mesh density without loss of the most important features of flow. Reynold's approximation is the starting point for this method. It assumes that at each moment the velocity of flow is the sum of the average velocity and the fluctuating component (equation 2):

$$u_i = \bar{U}_i + u_i^{'} \qquad i = x, y, z \tag{2}$$

The averaging of fluctuating component in time should definitely give a zero value:

$$\overline{u_i^{'}} = 0 \tag{3}$$

When applying it to the Navier – Stokes equation one obtains new formulation with new 6 unknown values, which form Reynolds viscous stress tensor. The problem can be now solved by application of the additional transport equation for each component of the tensor. However, it still requires intensive computing. To simplify it, Boussinesq's hypothesis is utilized, which states that the tensor components are expressed by a new variable – the turbulent viscosity (μ_T).

Considering this approach, energy transport under turbulent conditions is similar to molecular transport, apart from the fact that turbulent viscosity does not describe the fluid but is connected mostly with the character of flow. The *k*-epsilon (*k*-ε) model is one of the most popular variants of the RANS approach. Two quantities are most important here: *k* which expresses turbulence kinetic energy (4) and ε, which denotes rate of turbulence energy dissipation.

$$k = \overline{u_i^{'} u_i^{'}} / 2 \tag{4}$$

The *k*-ε model simulates the character of flow accurately enough for most engineering applications. Turbulent viscosity is here adopted as:

$$\mu_T = \rho C_\mu k^2 / \varepsilon \tag{5}$$

where C_μ — constant of turbulence,

To solve the gas outflow model that is introduced in this article, an improved model of *k*-epsilon was in use. It gives better results for simulations of gas streams, flows with vortices and for near wall flows (Shih et al., 1995) The value C_μ is variable and depends on *k*, ε, and velocity gradients.

2.2. Modeling air flow in goaf

The permeability of this porous zone was assumed to be anisotropic: with a high value along the direction towards the shaft, and a low value (equal to the permeability of sand) in both perpendicular directions.

The value of the longitudinal permeability was estimated using Darcy's law:

$$u = \frac{K}{\mu}\frac{\Delta p}{l} \tag{6}$$

where: K is permeability.

Then this formula was compared to the Darcy-Weisbach's equation:

$$\Delta p = \lambda \frac{l}{D}\frac{\rho u^2}{2} \tag{7}$$

For low values of Reynold's number (Re < 2100) the factor λ depends on the shape of the duct cross-section and Reynold's number: $\lambda = a$ / Re (a = 57 for square ducts).

The Reynold's number can be expressed as:

$$\mathrm{Re} = \frac{uD\rho}{\mu} \tag{8}$$

Finally, formula (17) can be rewritten as:

$$u = \frac{2D^2}{a\mu}\frac{\Delta p}{l} \tag{9}$$

Thus, taking into account formula (9), equivalent longitudinal permeability can be expressed as $K = 2D^2/a$. In engineering and science the permeability is often replaced by a new quantity – viscous resistance: this is simply the inverse of permeability.

3. The model

3.1. Determination of volume of goaf

Initially, the volume of goaf was based on analysis of mining maps. Then it was recalculated with application of Torricelli's flow model (Fig. 1) (equations 10-14). The main aim was to obtain the same velocity at the outlet as was measured *in-situ* (Wrona et al., 2016).

The following simplifications and assumptions were adopted:

- outflow occurs only under an atmospheric pressure drop, which is constant in time,
- the gas is regarded as ideal gas and the process is isothermal,
- gravity is not taken into account,
- any effects of turbulence are not taken into account,
- all underground excavations are represented by a cylindrical tank of given volume with a rectangular opening of actual area (Fig. 1),
- the velocity profile along the opening diameter is uniform.

– the initial atmospheric pressure was set at 98700 Pa, the barometric tendency of pressure drop was assumed to be 100 Pa/h (according to measurements).

Under the above assumptions the equation of state can be written as:

$$pV = const \tag{10}$$

After differentiation we obtain:

$$V\mathrm{d}p + p\mathrm{d}V = 0 \tag{11}$$

The constant pressure drop is expressed as (z is barometric tendency):

$$\mathrm{d}p = -z\mathrm{d}t \tag{12}$$

Since the pressure drops, the airflow increases. The average velocity u can be computed as:

$$\mathrm{d}V = Su\mathrm{d}t \tag{13}$$

$$u = \frac{V_0 z}{pS} \tag{14}$$

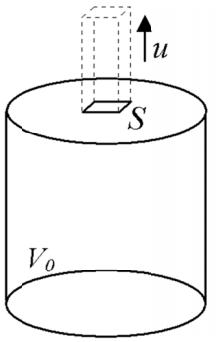

Fig. 1. The Torricelli's model

As can be seen (equation 14), gas velocity depends linearly on reservoir volume and the barometric tendency. As the result outlet velocity was 2.0 m/s and volume of the excavations was 540000 m^3 (S = 0.078 m^2).

3.2. Geometry

The following conditions (the same as determined during the measurements (Wrona et al., 2016) were assumed for further computing.

The model consists of two underground spaces (a shaft and a reservoir) linked by a corridor. The geometry is given in Figure 2. The length of the shaft is 498 m and the diameter is 7 m. The reservoir is flat and cuboid with dimensions 120 m × 10 m × 300 m and is located at a depth of 292 m.

Both elements are connected by a corridor with a length of 10 m. The cross-sectional area of the corridor is 2.5 m^2 and the corridor is filled with sand. The model under consideration has a symmetry plane to decrease the computational requirements.

The shaft is considered to be empty. To assure laminar flow in goaf, the space inside the reservoir is treated as an anisotropic porous zone. The viscous resistance coefficient is 10^6 $1/m^2$ (set across the corridor) and 7.0 $1/m^2$ (set along the corridor). Porosity is 1.0. The corridor is taken to be isotropic (the viscous resistance coefficient is 10^8 $1/m^2$; porosity is 0.4.

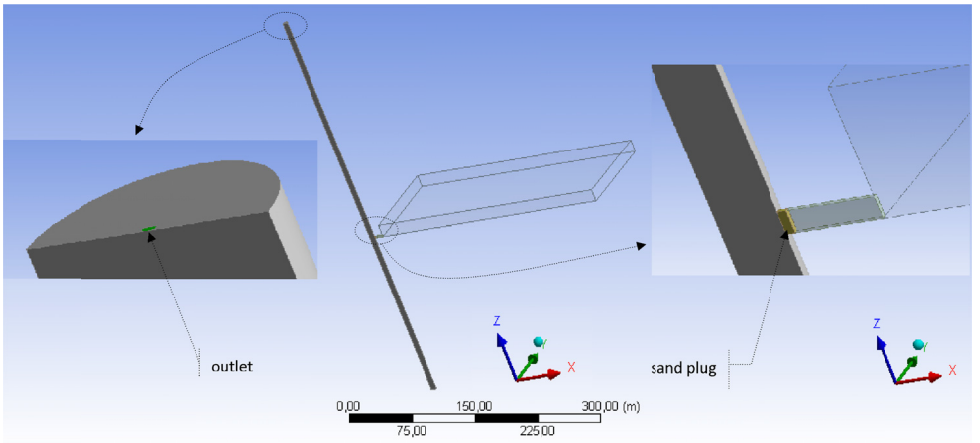

Fig. 2. The model structure

3.3. Mesh and solver

To avoid the problems of flow modeling a mesh was condensed for some locations (the outlet, the corridor).

Additionally, 5 inflation layers were added to the shaft surfaces to enhance the accuracy at the boundary. The total number of cells was 369593. The mesh minimum orthogonal quality was 0.11, while the lowest value acceptable for calculations is 0.1. The ambience was modeled by a pressure outlet boundary condition. The *k*-epsilon realizable turbulence model was applied.

The time step as adjusted to 1s. This was possible due to very slow pressure changes. It may be stated that a short time interval causes calculations to take longer. However, the following inequality (Courant-Friedrichs-Lewy condition) must be fulfilled:

$$C = \frac{u\Delta t}{\Delta x} \leq C_{\max} \tag{15}$$

This inequality describes the relationship between fluid velocity (u), typical mesh size (Δx) and time step (Δt). $C_{\max}$ is the Courant number and should not be significantly greater than 1 (the exact value of $C_{\max}$ depends on solver details).

The maximum number of iteration per time step was set at 20, which is the default value, ensuring solution convergence. The summary of the numerical model is shown in Table 1.

TABLE 1

Numerical model summary

Feature		Value
Turbulence model		*k*-epsilon realizable
Fluid material		Air (ideal gas)
Operating pressure		98700 Pa
Gravitational acceleration		9.81 m/s^2
Solver		Pressure based
Pressure / velocity coupling		Simple
Under-relaxation factors	Pressure	0.1
	Momentum	0.1
	Energy	0.95
	Others	Default
Time step		1 s

The calculations were done in transient mode using a standard PC computer with Intel Core i7 CPU 2.2 GHz and 8 GB RAM.

3.4. Flow and air parameters

The ambient temperature was equal to the recorded value (15°C). The following temperature profile was assumed: 281 K at the depth of 4 m, followed by an increase of 1 K per 33 m according to the average geothermal gradient in the Silesian area (Kurowska, 1999). The temperature profile is shown in Figure 3. In addition, the density profile of the gases is shown in the same figure.

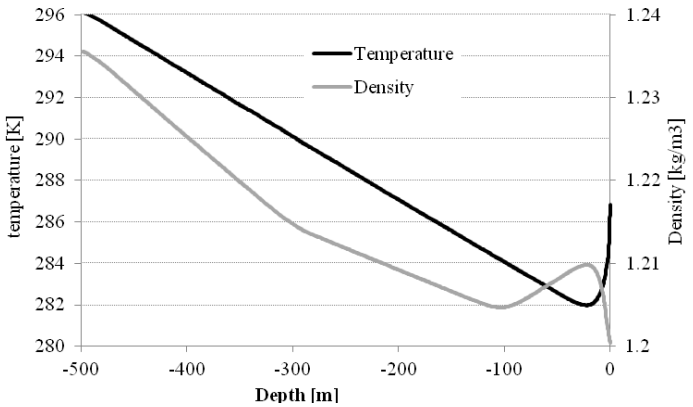

Fig. 3. Air temperature and density profiles

Vertical profiles of O_2 and CO_2 (Fig. 4) were initially assumed according to Grzybek (Grzybek, 2012).

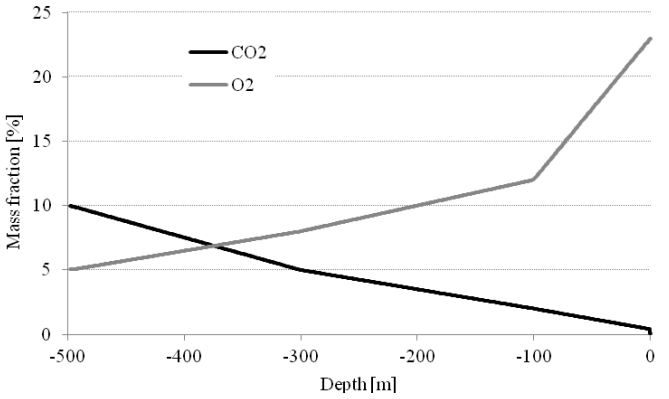

Fig. 4. Vertical profiles of O_2 and CO_2 concentration

3.5. Modeling the barometric tendency

Since the atmospheric pressure changes continuously and this process is rather slow, pressure changes can be approximated by linear sections. However, due to unrealistic rapid changes of the barometric tendency at transition points this causes unwanted disturbances in the simulation process. To avoid this, the barometric tendency was modeled by the use of Bezier curves. A Bezier curve is defined by a set of control points. Equation 16 shows the parametric form of a Bezier curve. The curve passes through the first and last points, the intermediate points control the shape of the curve (Fig. 5).

$$p(t) = \sum_{i=0}^{n} p_i B_i^n(t), \quad t \in [0,1] \tag{16}$$

where:

$p(t)$ — a point on the curve,
p_i — i–th control point,
n — number of control points,
t — control parameter,
B_i^n — i–th Bernstein basis polynomial (Equation 23).

$$B_i^n(t) = \binom{n}{i} t^i (1-t)^{n-i} \tag{17}$$

3.6. Output data

During the simulation the following quantities were recorded every 10 time steps with averaging over 10 time steps:

- ambient pressure,
- total mass flow rate through the outlet,
- mass flow rate of CO_2,
- averaged outlet velocity.

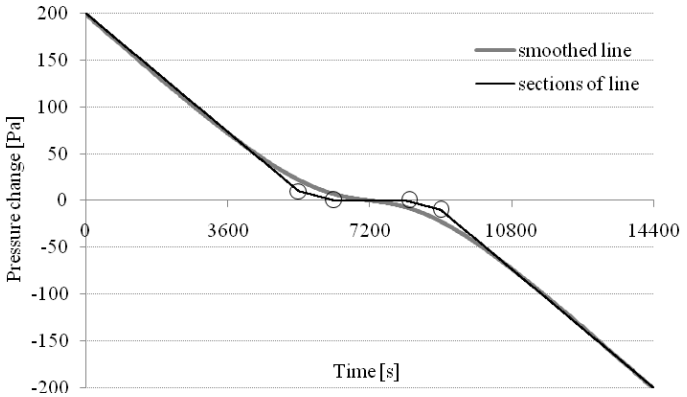

Fig. 5. Barometric tendency modeled with the use of Bezier curves (the transition points are marked)

3.7. Validation

The results of the simulation were compared to the results obtained during measurements (e.g. Wrona et al., 2016). The comparison is presented in Figure 6.

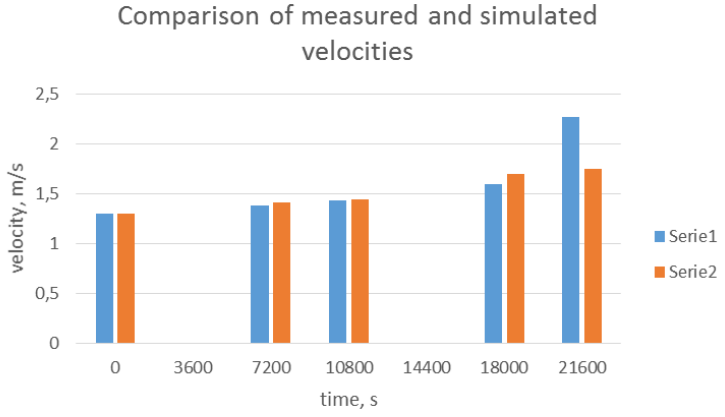

Fig. 6. Comparison of measured and simulated values of outlet velocity, serie 1 – measured, serie 2 – simulated

4. The results and discussion

Three scenarios of barometric tendency variations were assumed:

a) a constant increase of 0.5 hPa/h before the pressure drop period,
b) a constant decrease of 0.5 hPa/h before the pressure drop with a different BT,
c) a constant increase of 0.5 hPa/h after the pressure drop period.

As it can be observed in Fig. 7-16 the lines of pressure drop were modeled with the use of Bezier curves (described in chapter 3.5).

4.1. Airflow and air velocity

The visualizations of the assumed changes of pressure and the calculated total mass flow rates are presented in Figures 7, 8 and 9. Positive values mean that the direction of flow is towards the underground site; negative values mean that emission to the surface occurs. The vertical dotted line separates two different pressure tendencies in a scenario (it starts at 18000s for each case).

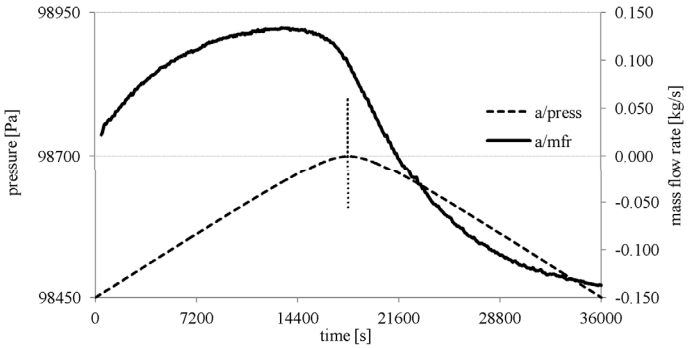

Fig. 7. Barometric tendency and mass flow rate for scenario "a"

Figure 7 clearly shows inert behavior of the process. It was assumed that pressure rises and then started to fall (scenario "a"). After a change of BT (at 18000s of the simulation) (Fig. 7) the airflow changed its direction 3600 s (1 hour) after the change of BT. At 36000 s the total mass flow rate was 0.137 kg/s (with the direction to the surface), (carbon dioxide rate CO_2 was 9.39 10^{-4} kg/s).

As it can observed the maximum of mass flow rate precedes the moment of change of BT. This observation and the overall direction and behavior of mass flow rate curve can be explained as follows:

- The simulation starts from a steady state, then the pressure drop forces the outflow of the gases, but this process involves gradual acceleration of entire mass of gases inside the shaft and excavation. Therefore the value of mass flow rate becomes higher at the beginning.
- Then, the process reaches almost the steady state and then the BT begins to slow down. As the pressure curve is very smooth, it is difficult to notice that the maximum of flow rate coincides with the very beginning of change of BT. However, this phenomenon requires additional works to be explained in details.

For scenario "b" (Fig. 8) there was an assumption of pressure falling at constant rate (hPa/h). constant pressure drop.

The mass flow rate strongly depends on BT variations. It can be observed especially at 14400 s. As it was stated in chapter 3.5, to avoid rapid changes of the barometric tendency at transition points Bezier curves were applied and it led to slight fluctuation of pressure line at 18000 s.

Every change of BT is followed by significant jump or drop of flow rate. Although, similarly as for Fig. 7, this phenomenon is worthy to be deeply examined in the future work.

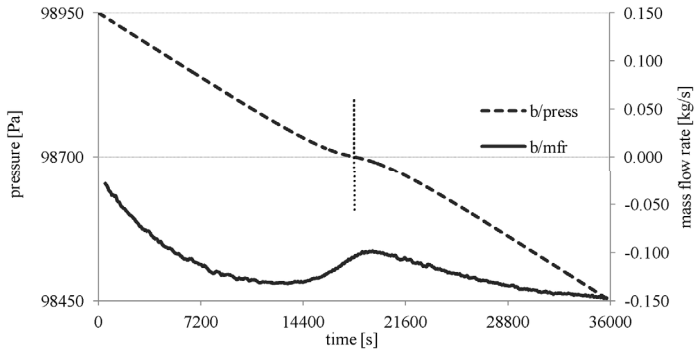

Fig. 8. Barometric tendency and mass flow rate for scenario "b"

The maximal total mass flow rate was 0.147 kg/s (carbon dioxide rate was CO_2 11.5 10^{-4} kg/s) with the direction to the surface. It can be observed that in spite of the same value of final pressure (98450 Pa after 36000 seconds of simulation) total mass flow rate and carbon dioxide rate at this time were larger as under scenario "a".

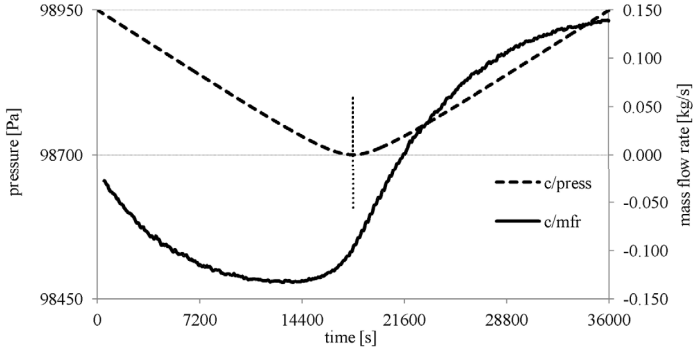

Fig. 9. Barometric tendency and mass flow rate for scenario "c"

For scenario "c" (Fig. 9) the airflow changes its direction 3600 seconds after a change of BT. The maximal total mass flow rate was 0.132 kg/s (carbon dioxide rate CO_2 was 8.1 10^{-4} kg/s) (at about 14000 s with the direction to the surface). It's another example of inert behavior of examined process.

Figures 10, 11 and 12 show the relation between barometric tendency and calculated outlet velocities. Positive values indicate that the direction of flow is to the surface; negative values indicate gas flow to the underground site. Similarly as in Fig. 7-9 for scenarios "a" and "c" change of flow direction can be noticed at 21600 s of simulation.

For scenario "a" (Fig. 10), the maximal velocity was 1.67 m/s (flow direction to the surface) and 1.44 m/s (flow to the underground site).

For scenario "b" (Fig. 11), the maximal velocity was 1.79 m/s at 36000 s into the simulation. The flow direction was to the surface during entire time of simulation.

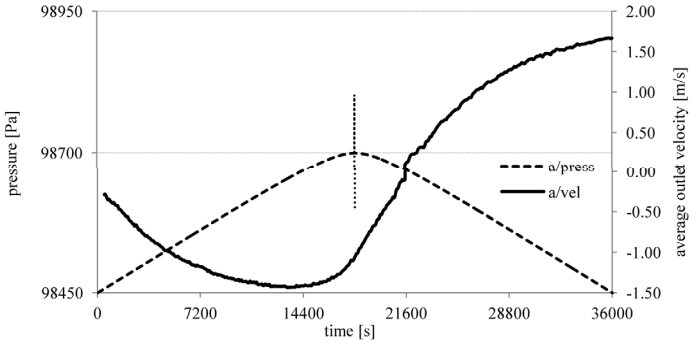

Fig. 10. Barometric tendency and outlet velocity for scenario "a"

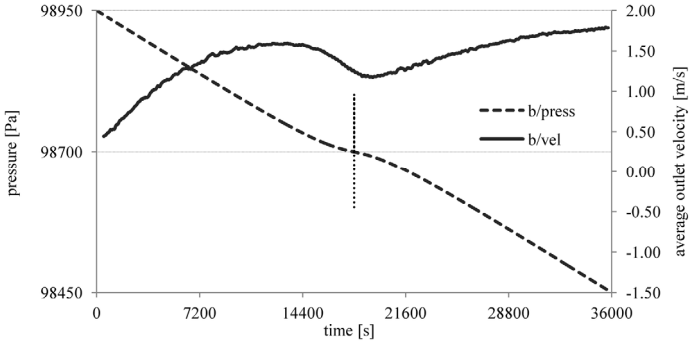

Fig. 11. Barometric tendency and outlet velocity for scenario "b"

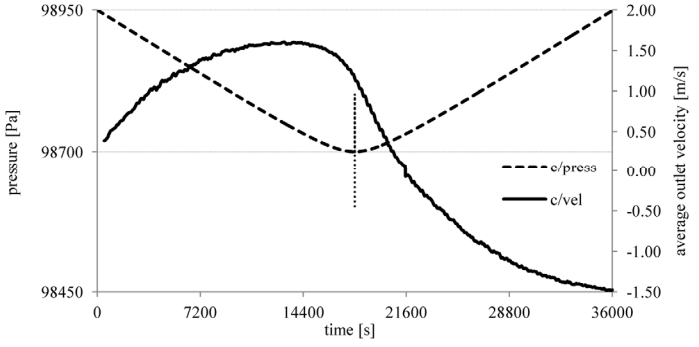

Fig. 12. Barometric tendency and outlet velocity for scenario "c"

For scenario "c" (Fig. 12), the maximal velocity was approximately 1.50 m/s for both directions.

Figures 13-15 show the relation between barometric tendency and the calculated mass fraction of CO_2. A rapid jump and further fluctuations in the CO_2 mass fraction were observed at

21600 s into the simulation. This was when the flow changed its direction. The highest velocity was reached for scenario "b" – according to longer time of pressure drop.

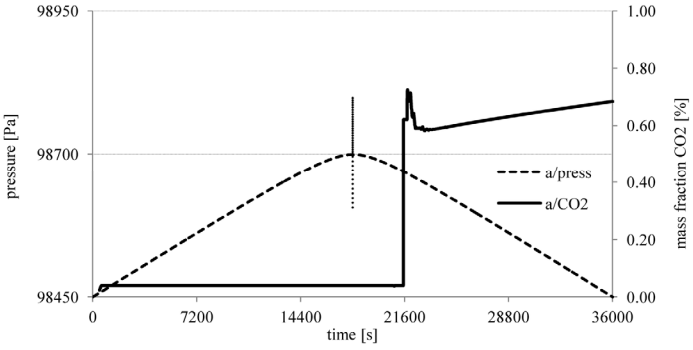

Fig. 13. Barometric tendency and mass fraction of CO_2 for scenario "a"

Figure 13 shows inert behavior of the process which can lead to incorrect interpretations of measurement results. In this case gas detection conducted above a shaft during the first phase of pressure drop period (between 18000 s and 21600 s) will not indicate CO_2 presence.

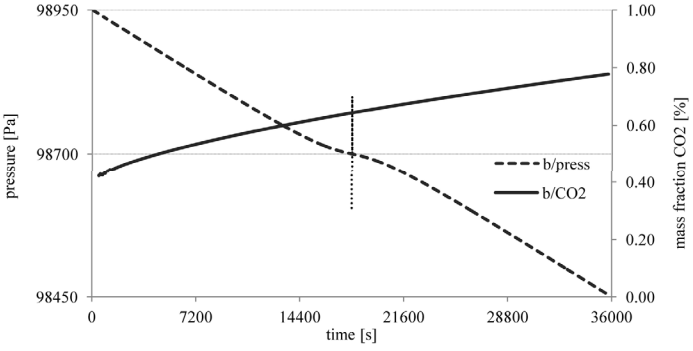

Fig. 14. Barometric tendency and mass fraction of CO_2 for scenario "b"

This scenario shows constant increase of CO_2 concentration in gas mixture emitted from a shaft. maximal CO_2 concentration obtained during scenario "b" was 0,78% (by mass).

An inertia phenomenon was also observed for scenario "c". After the reversion of the barometric tendency, the gases kept flowing toward the surface for about an hour. CO_2 emissions can be still detected despite of pressure increase (Fig. 15-16).

The amount of CO_2 which is emitted during pressure increase period can be estimated by taking into account the shaded area in Figure 16. It was estimated at 1.11 kg.

However, the *in situ* measurements reported a higher mass fraction of CO_2. This led to a correction in the vertical profile of CO_2 concentration. The alternative profile of CO_2 concentration was assumed as in Figure 17. The vertical profile of O_2 remained the same.

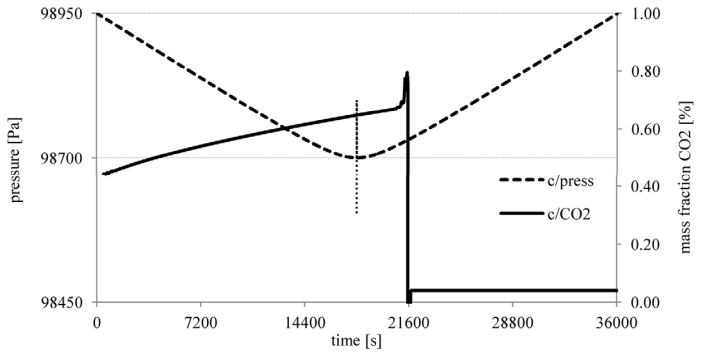

Fig. 15. Barometric tendency and mass fraction of CO_2 for scenario "c"

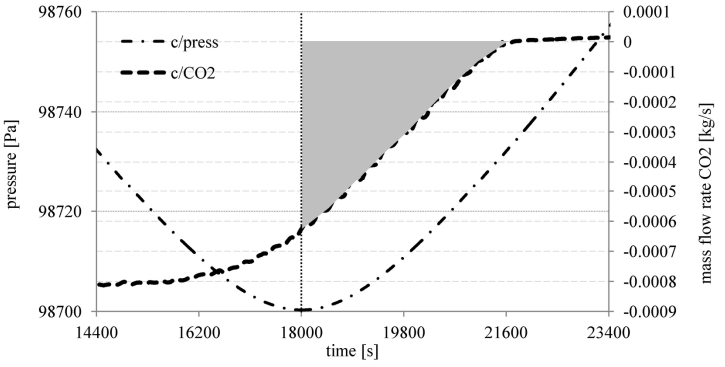

Fig. 16. CO_2 outflow in the time interval just after BT reversion

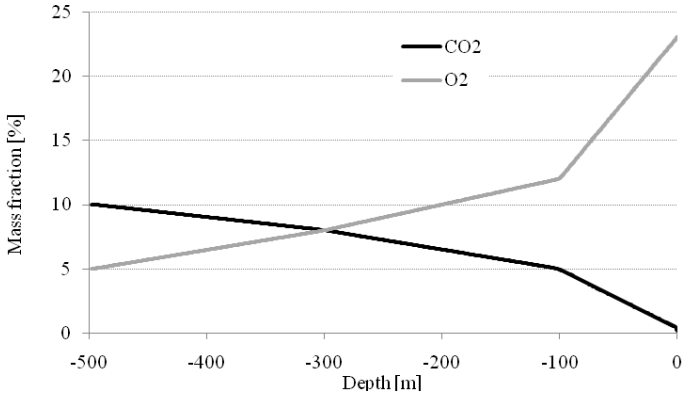

Fig. 17. Modified vertical profile of CO_2 concentration; unchanged profile of O_2 concentration

Variations in CO_2 concentration at the outlet were simulated for the "b" scenario, extended to 72000 s. The results are presented in Figure 18

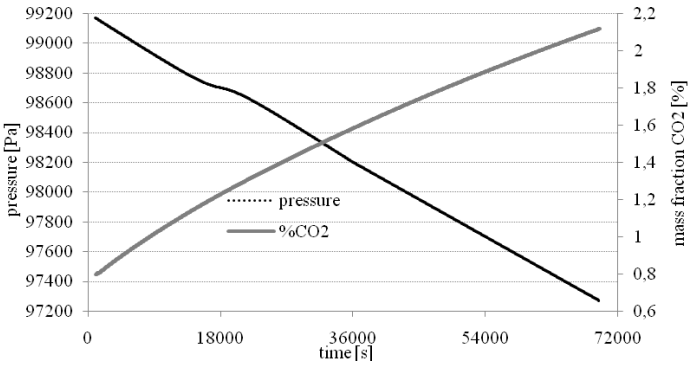

Fig. 18. Barometric tendency and CO_2 concentration for scenario "b", extended to 72000 s for modified vertical profile of CO_2 concentration and unchanged profile of O_2 concentration

After modification of initial CO_2 profile and after extension of simulation time to 72000 seconds maximal CO_2 concentration was 2.18% what is comparable to results obtain during real *in situ* tests.

4. Conclusions

1. The main aim of undertaken research was to prove that process of gas emissions from underground sites is inert. It means that under particular circumstances gas emissions can be detected even at initial phase of pressure rise or cannot be detected during pressure drop.

The result for scenarios "a" and "c" clearly showed mentioned behavior of gases.

2. For the "a" and "c" scenarios, a change in the baric tendency (from negative to positive and vice versa) led to a change in airflow direction. For this particular example, the change lasts for 3600 s (one hour). It proves that CO_2 emissions may be expected even during a pressure rise period (scenario "c"). The results from scenario a) proved that when pressure begins to drop after a rise period, for a certain time period (3600 s) CO_2 emissions are not detected.

3. For scenario "b", when pressure fall lasting 72000 s, it was stated that at the end of the simulation CO_2 concentration was 2.18%vol. At 3600 s the CO_2 concentration was 1.4%vol. and the CO_2 mass flow rate was 0.15 kg/s. Taking into account greenhouse gas emissions the figure was 514 kg_{CO2}/h.

4. The maximal velocity of gas emissions was detected under the "b" scenario, with a value of 1.8 m/s at 36000 s into the simulation.

Acknowledgments

Appreciations for Mr. Tim Harrell for English proof reading of the text.

References

Annunziatellis A., Beaubien S.E., Bigi S., Ciotoli G., Coltella M., Lombardi S., 2008. *Gas migration along fault systems and through the vadose zone in the Latera caldera (central Italy): implications for CO_2 geological storage*. Int. J. Greenh. Gas Control **2** (3/2008), p. 353-372, doi:10.1016/j.ijggc.2008.02.003.

Bateson L., Vellico M., Beaubien S.E., Pearce J.M., Annunziatellis A., Ciotoli G., Coren F., Lombardi S., Marsh S., 2008. *The application of remote-sensing techniques to monitor CO_2-storage sites for surface leakage: method development and testing at Latera (Italy) where naturally produced CO_2 is leaking to the atmosphere*. Int. J. Greenh. Gas Control **2** (3/2008), p. 388-400, doi:10.1016/j.ijggc.2007.12.005.

Beaubien S., Jones D., Gal F., Barkwith A., Braibant G., Baubron J.-C., Ciotoli G., Graziani S., Lister T., Lombardi S., 2013. *Monitoring of near-surface gas geochemistry at the Weyburn, Canada, CO_2-EOR site, 2001-2011*. Int. J. Greenh. Gas Control **16**, p. 236-S262, doi: 10.1016/j.ijggc.2013.01.013.

Cheng Y.-P., Wang L., Zhang X.-L., 2011. *Environmental impact of coal mine methane emissions and responding strategies in China*. Int J Greenh Gas Control **5** (1/2011), p. 157-166. doi:10.1016/j.ijggc.2010.07.007.

Dziurzyński W., Krawczyk J., Krach A., Pałka T., 2008. *Computer simulation of air and methane flow following an outburst in transport gallery D-6, bed 409/4*. Journal of the South African Institute of Mining and Metallurgy **108**, 3, p. 139-145.

Eicker H., 1987. *Verlauf und Beherrschung der Ausgasung abgeworfener Grubengebaude*. Gluckauf-Forschungshefte **48**, 6, p. 324-328.

Feitz A., Jenkins C., Schacht U., Mcgrath A., Berko H., Schroder I., Noble R., Kuske T., George S., Heath C., Zegelin S., Curnow S., Zhang H. Sirault X. Jimenez-Berni J. Hortle A., 2014. *An assessment of near surface CO_2 leakage detection techniques under Australian conditions.* Energy Procedia **63**, p. 3891-3906, doi:10.1016/j.egypro.2014.11.419.

Geurts B., 2003. *Elements of direct and large-eddy simulation*. R.T. Edwards Inc. ISBN-13: 978-1930217072

Grzybek I., 2012. *Studium uwarunkowań emisji gazów ze zlikwidowanych kopalń SW części GZW*. Bezpieczeństwo Pracy i Ochrona Środowiska w Górnictwie, no. 1-5, 8-10 (in Polish).

Herrán-González A., De La Cruz J.M., De Andrés-Toro B., Risco-Martín J.L., 2009. *Modeling and simulation of a gas distribution pipeline network*. Applied Mathematical Modelling **33**, 3, p. 1584-1600, doi:10.1016/j.apm.2008.02.012.

Jones D.G., Barkwith A.K.A.P., Hannis S., Lister T.R., Gal F., Graziani S., Beaubien S.E., Widory D., 2014. *Monitoring of near surface gas seepage from a shallow injection experiment at the CO_2 Field Lab, Norway*. International Journal of Greenhouse Gas Control **28**, p. 300-317, doi:10.1016/j.ijggc.2014.06.021.

Koyama T., Niretnieks I., Jing L., 2008. *A numerical study on differences in using Navier-Stokes and Reynolds equations for modeling the fluid flow and particle transport in single rock fractures with shear*. International Journal of Rock Mechanics and Mining Sciences **45**, 7, p. 1082-1101, doi:10.1016/j.ijrmms.2007.11.006.

Kurowska E., 1999. *Disturbance of geothermal field of the Upper Silesian Coal Basin due to mining activity*. Bulletin d'Hydrogcologie, no I7, Centre d'Hydrogiologie, Universitc de Neuchdte.

Lagny C., Lafortune S., Charmoille A., Pokryszka Z., Degrelle F. Kimmel M., 2013. *Understanding CO_2 Gas Production Above a Partly Flooded. Former Coal Mining Area*. Procedia Earth and Planetary Science **12**, p.7-16, doi: 10.1016/j.proeps.2013.03.095.

Lewicki J.L., Birkholzer J., Tsang C.-F., 2007. *Natural and industrial analogues for leakage of CO_2 from storage reservoirs: identification of features, events, and processes and lessons learned*. Environ. Geol. **52**, p. 457-467, doi:10.1007/s00254-006-0479-7.

Lunarzewski L., 2010. *Coal mine gas predictor*. 10th Underground Coal Operators Conference, University of Wollongong & the Australasian Institute of Mining and Metallurgy, p. 247-256.

Oldenburg C.M., Lewicki J.L., Dobeck L., Spangler L., 2010. *Modeling gas transport in the shallow subsurface during the ZERT CO2 release test*. Transp. Porous Media **82** (1), p. 77-92, doi:10.1007/s11242-009-9361-x.

Paulley A., Metcalfe R., Egan M., Maul P.R., Limer L., Grimstad A.-A., 2013. *Hypothetical impact scenarios for CO_2 leakage from storage sites*. Energy Proc. **37**, p. 3495-3502, doi:10.1016/j.egypro.2013.06.240.

Pawar R., Theresa J., Watson L., Gablea C.W., 2009. *Numerical simulation of CO_2 leakage through abandoned wells: model for an abandoned site with observed gas migration in Alberta, Canada*. Energy Proc. **1**, p. 3625-3632, doi:10.1016/j.egypro.2009.02.158.

Perera M.S.A., Ranjith P.G., Choi S.K., Airey D., 2011. *Numerical simulation of gas flow through porous sandstone and its experimental validation*. Fuel **90**, 2, p. 547-554, doi:10.1016/j.fuel.2010.09.029.

Shih T.H., Liou W.W., Shabbir A., Yang Z., Zhu J., 1995. *A New k-ε Eddy Viscosity Model for High Reynolds Number Turbulent Flows-Model Development and Validation*. Computers Fluids **24**, p. 227-238.

Schroder I.F., Zhang H., Zhang C., Feitz A.J., 2016. *The role of soil flux and soil gas monitoring in the characterization of a CO_2 surface leak: A case study in Qinghai, China*. International Journal of Greenhouse Gas Control **54**, Part 1, p. 84-95, doi:10.1016/j.ijggc.2016.07.030.

Vreman B., Geurts B., Kuerten H., 1997. *Large eddy simulation of turbulent mixing layer*. J. Fluid Mech. **339**, p. 357-390. doi:10.1017/S0022112097005429.

Wrona P., Różański Z., Pach G., Suponik T., Popczyk M., 2016. *Closed coal mine shaft as a source of carbon dioxide emissions*. Environmental Earth Sciences **75**, 15, art. no. 1139, p. 1-12. DOI: 10.1007/s12665-016-5977-7.